AGU PUBLICATIONS

JGR

Journal of Geophysical Research: Earth Surface

RESEARCH ARTICLE

10.1002/2014JF003250

Key Points:
- The seismology of a floating iceberg is observed in a rare field deployment
- Cross-correlation analysis reveals iceberg noise generation and propagation
- Iceberg collisions (part of breakup process) radiate hydroacoustic noise

Supporting Information:
- Readme
- Movie S1

Correspondence to:
D. R. MacAyeal,
drm7@uchicago.edu

Citation:
MacAyeal, D. R., Y. Wang, and E. A. Okal (2015), Ambient seismic, hydroacoustic, and flexural gravity wave noise on a tabular iceberg, *J. Geophys. Res. Earth Surf.*, *120*, 200–211, doi:10.1002/2014JF003250.

Received 16 JUN 2014
Accepted 15 JAN 2015
Accepted article online 19 JAN 2015
Published online 12 FEB 2015

Ambient seismic, hydroacoustic, and flexural gravity wave noise on a tabular iceberg

Douglas R. MacAyeal[1], Yitan Wang[2], and Emile A. Okal[3]

[1]Department of Geophysical Sciences, University of Chicago, Chicago, Illinois, USA, [2]Physical Sciences Division, University of Chicago, Chicago, Illinois, USA, [3]Department of Earth and Planetary Sciences, Northwestern University, Evanston, Illinois, USA

Abstract Cross correlation of ambient seismic noise between four seismographs on tabular iceberg C16, Ross Sea, Antarctica, reveals both the source and the propagation characteristics of signals associated with icebergs. We find that noise correlation functions computed from station data are asymmetric about zero time lag, and this indicates that noise observed on the iceberg originates primarily from a compact, localized source associated with iceberg collisions between C16 and a neighboring iceberg, B15A. We additionally find two, and possibly more, distinct phases of noise propagation. We believe that flexural gravity wave propagation dominates the low-frequency noise (>10 s period) and that hydroacoustic wave propagation in the water column between the ice and seabed appears to dominate high-frequency noise (>10 Hz). Faster seismic propagation dominates the intermediate band (2–6 Hz); however, we do not have sufficient data to characterize the wave mechanisms more precisely, e.g., by identifying distinct longitudinal and shear body waves and/or surface waves. Secular changes in the amplitude and timing of ambient noise correlations, e.g., a diurnal cycle and an apparent shift in the noise correlation of fast seismic modes between two periods of the deployment, allow us to speculate that ambient noise correlation analysis may be helpful in understanding the sources and environmental controls on iceberg-generated ocean noise as well as geometric properties (such as water column thickness) of subglacial lakes.

1. Introduction

In an effort to identify the source mechanism of hydroacoustic tremor observed at South Pacific Islands [e.g., *Talandier et al.*, 2002, 2006], four seismic stations were deployed on iceberg C16 over a 60 day period in December 2003 and January 2004 (Figure 1). Iceberg C16 was calved from the western end of the Ross Ice Shelf in 2000 following a collision with iceberg B15A [*MacAyeal et al.*, 2008a]. At the time of the deployment, it was approximately 50 to 75 m thick, 45 km long, and 25 km wide. During the deployment, C16 was aground against Ross Island and was adjacent to several freely moving icebergs, B15A and B15J, that gyrated with the ocean tide in the wind shadow of Ross Island, repeatedly colliding with C16 as a result of wind-driven and tidal oscillations. Analysis of the seismic data showed that these iceberg collisions were indeed the source of tremor signals identical in character to those observed in the South Pacific and involved a stick-slip mechanism associated with the glancing, scraping movement of one iceberg along the edge of the other [*MacAyeal et al.*, 2008b].

The seismometer deployment on the iceberg also revealed that the surface ocean environment surrounding both grounded and moving icebergs is extremely noisy, involving hundreds of episodes of tremor associated with iceberg collisions and other less defined events presumably linked to the calving of small iceberg fragments from the edges of the large tabular icebergs. A dominant feature of this noise was its lack of discrete, impulsive icequake-like events. Without such discrete events, it is impractical to characterize the noise further using traditional arrival time and ground motion observations to deduce source characteristics and propagation modes.

To better characterize the iceberg noise in the absence of icequake-like events, we resorted to noise correlation techniques that are emerging in treatments of seismic arrays deployed for the study of the lithosphere [e.g., *Hadziioannou et al.*, 2011]. This technique has been successfully used on the Amery Ice Shelf to deduce Rayleigh wave propagation characteristics in the ice and firn as well as hydroacoustic resonance characteristics of the ocean layer below the ice shelf [*Zhan et al.*, 2014]. *Zhan et al.* [2014] intended to determine whether noise correlation analysis could be used for ambient noise tomography

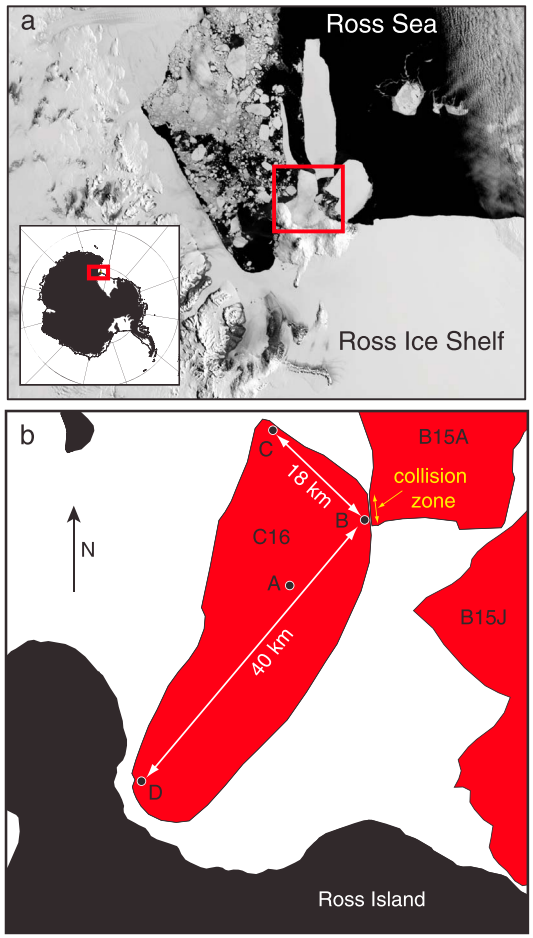

Figure 1. Icebergs in the Ross Sea, Antarctica. (a) Moderate Resolution Imaging Spectroradiometer (MODIS) satellite image of the Ross Island region of the Ross Sea at 18:40 UTC on 26 December 2003. Inset shows location in Antarctica; red box shows zoomed sketch map of Figure 1b. (b) Iceberg C16 with seismometer stations A–D and collision zone.

[e.g., *Shapiro et al.*, 2005]. This is particularly suitable in physical situations where the ambient noise is radiating isotropically through the region of study, because in this circumstance, station pair noise correlation functions tend to converge to the impulse response functions for an impulse at one station being observed at the other. In cases where the ambient noise is not isotropic, noise correlation is still useful for resolving and monitoring seismic wave speeds [e.g., *Hadziioannou et al.*, 2011]. The objective of our study is to examine the process and utility of cross-correlating seismic records from an array of stations on an iceberg (Figure 1). The intention is to evaluate whether ambient noise correlation analysis can provide useful information relating to the physical and environmental conditions that characterize an iceberg.

2. Data and Methods

Four seismic stations, C16A, C16B, C16C, and C16D, were established on iceberg C16 in mid-November 2003 by helicopter support from McMurdo Station. All four stations operated simultaneously for a 28 day period from 13 December 2003 to 4 January 2004. Stations C16A and C16B operated simultaneously for a total of 50 days, from 4 December 2003 to 22 January 2004. All stations were equipped with Guralp CMG-40T intermediate-band seismometers (flat response to velocity from 30 s to 50 Hz) set up to record vertical (Z), North (N), and East (E) ground motions (data channels) at two separate sample rates, 100 Hz and 1 Hz. (Data channels are referred to as HHZ, HHN, and HHE for the 100 Hz sample rate and LHZ, LHN, and LHE for the 1 Hz sample rate.) One station, C16A, was additionally fitted with a Streckeisen STS 2 seismometer (flat response to velocity from 120 s to 10 Hz).

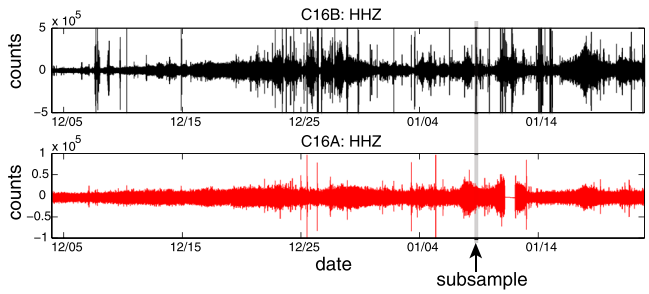

Figure 2. Seismograms of HHZ channels for C16A and C16B (subsampled at 2 Hz) for a 50 day period. Arrow and shaded stripe indicate subsample shown in Figure 3. The seismograms express ground velocity, but because only relative ground motion amplitude is of interest here, they are shown in the scaled units (counts) directly output by the instruments.

Unfiltered seismograms of the HHZ channels for C16A and C16B for the full 50 day period (subsampled at 2 Hz) are shown in Figure 2. The seismogram from C16B is generally much noisier and reflects higher-amplitude ground motion than that from C16A. This corresponds with the fact, known a priori, that C16B was located near the edge of the iceberg that repeatedly collided with neighboring iceberg B15A [*MacAyeal*

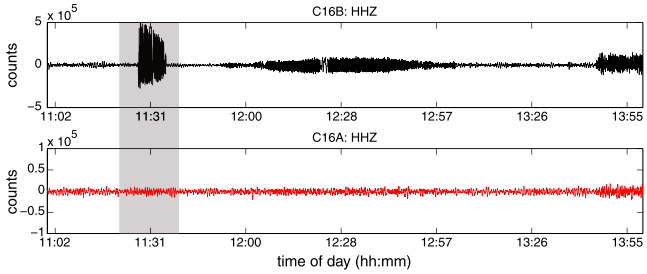

Figure 3. Seismograms of HHZ channels for C16A and C16B (subsampled at 2 Hz) for a 3 h period on 6 January 2004. Shaded box indicates subsample shown in Figure 4.

et al., 2008a]. The collision zone on both icebergs showed evidence of extraordinary damage, visible as "push mound" features [*MacAyeal et al.*, 2008a] where firn and ice were displaced from the battered edge of the iceberg up onto the iceberg's original upper surface. A webcam was set up along the collision zone near C16B to document the collisions, and its imagery is available as a time lapse video (Movie S1) in the supporting information (see also website http://thistle.org/iceberg/index.shtml).

To illustrate the noisy nature of the seismograms caused by the repeated iceberg collisions, we show short subsets of the seismograms of C16A and C16B (unfiltered HHZ channels) in Figures 3 and 4. These subsets illustrate how the seismograms tend to be filled with events that appear on C16B but that are difficult to identify unambiguously on C16A. Often, where signals can be identified in both records, they have ambiguous start and stop phases that make it difficult to determine time differences associated with phase propagation from one station to another. This is because the majority of signals in C16B's seismogram is iceberg tremor [*MacAyeal et al.*, 2008b], which consists of hundreds to thousands of short stick-slip events generated by the colliding icebergs. Tremor differs from traditional impulsive icequake seismic sources by being emergent rather than impulsive and abrupt. Only by the fortuitous presence of an aseismic "eye" in two or three tremor episodes, possessing distinct restart events that could be correlated across stations, were the signals of iceberg tremor interpreted by *MacAyeal et al.* [2008b]. *MacAyeal et al.* [2008b] concluded from the analysis of the restart phase after the aseismic eye of the tremor that four phases of propagation were evident from the iceberg's seismometer array from seismometers deployed on neighboring Ross Island. Two modes of propagation, with phase speeds of 2925 $\pm$ 20 and 1690 $\pm$ 20 m s^{-1}, were identified as being *P* and *S* waves propagating within the iceberg. A hydroacoustic phase was identified with a phase speed of 1425 $\pm$ 20 m s^{-1}. The Ross Island seismometers displayed a head wave, where the hydroacoustic wave was converted to a solid earth *P* wave in the ocean bottom, with a net phase speed of 4475 $\pm$ 50 m s^{-1}.

The principal motivation for considering noise correlation methodology in processing the signals from the seismometer deployment on C16 is primarily that the seismic signals on the iceberg are strong and dominated by tremor. We define the noise correlation function (which we shall also refer to as the cross-correlation function), $\mathcal{X}_{i,j}[A, B, \mathcal{T}_n](\Delta t)$, as a function of time lag Δt that is parameterized by seismic channels (i, j are pairs of seismic data channels HHE, HHN, or HHZ), seismic stations being correlated (A, B are pairs of C16A, C16B, C16C, and C16D), and by the time window over which the noise correlation is evaluated ($t \in \mathcal{T}_n$, where t is time and $\mathcal{T}_n$ is a time window, either 2 h or 1 day in this study):

$$\mathcal{X}_{i,j}[A, B, \mathcal{T}_n](\Delta t) = \frac{1}{\sigma_n} \int_{t \in \mathcal{T}_n} d_i[A](t + \Delta t) \cdot d_j[B](t)\, dt \quad (1)$$

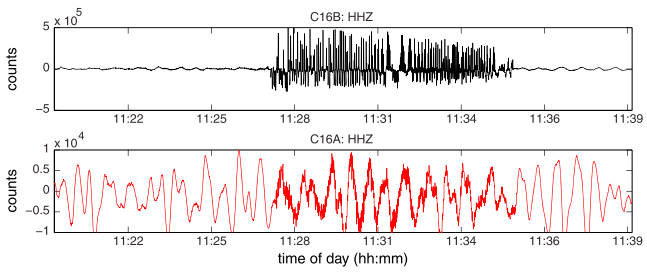

Figure 4. Seismograms of HHZ channels for C16A and C16B (subsampled at 2 Hz) for a 20 min period on 6 January 2004.

where, for example, $d_i[A](t)$ denotes data from the ith channel from station A and subscript n designates the time window. The functions are normalized by the standard deviation of $\mathcal{X}_n(\Delta t)$ within each time period, designated by σ_n. This renders the noise correlation functions dimensionless. We also produced average noise correlation functions, $\bar{\mathcal{X}}$, covering the entire time period of data collection by taking the arithmetic mean of the $\mathcal{X}_n$ values over all the time windows $\mathcal{T}_n$.

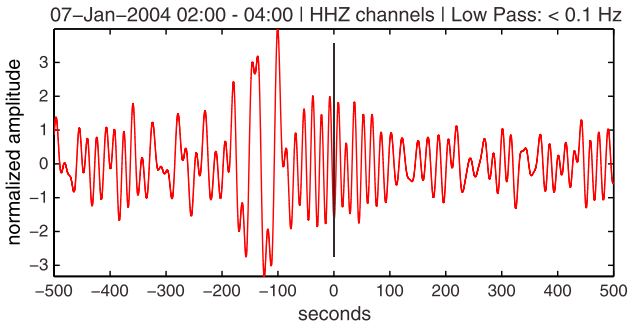

Figure 5. Noise correlation function $\mathcal{X}$ (nondimensional) for a 2 h time window on 7 January 2014 between stations C16B and C16A and low pass filtered to < 0.1 Hz. C16A's noise appears to have an approximately 100 s lag relative to that for C16B in this example, as is evident from the large-amplitude signal with periodicity of approximately 50 s aligned to the left of $\Delta t = -100$ s. Additional support for our interpretation of this signal can be seen in Figure 8.

Noise correlation functions were computed for all three channels (HHZ, HHN, and HHE) and all four stations. Because the function is symmetric with respect to station pairs, this computation determines 66 independent noise correlation functions for each time window [*Wang*, 2014]. The MATLAB routine *xcorr( )* was used to perform the computations for the $\mathcal{X}$' s using parameter setting "coeff" to scale the resulting function. To better visualize the noise correlation patterns, we normalized the $\mathcal{X}$' s in plots (shown in the following sections) using the standard deviation. Following *Zhan et al.* [2014], we adopt the convenience of using the channel data $d_i[A](t)$ directly, without first processing it to remove instrument response characteristics.

Once computed, the noise correlation functions are time filtered, using standard MATLAB finite impulse response (FIR) routines for low-band and high-pass filtering, and plotted as functions of Δt to investigate the signals that may be evident within the iceberg's noise field. In our interpretation of the noise correlation functions, we focus primarily on the time series of noise correlations that are generated for the n time window periods $\mathcal{T}_n$ and on the average, or stacked, version of all the noise correlation time windows. In the latter case, we compute the noise correlation using 1 day time windows and average the result over all the windows (days of the deployment).

3. Results

Example noise correlation functions from a single (arbitrary) 2 h time window are shown in Figures 5–7. These example functions are filtered into three frequency bands: less than 0.1 Hz, 2–6 Hz, and greater than 10 Hz. The most notable characteristic of the noise correlation functions in each of the three frequency ranges is their one-sided asymmetry, i.e., they are not symmetric about $\Delta t = 0$. This implies that the noise field is strongly directional rather than isotropic and means that the noise correlation functions are not convergent toward impulse response functions such as is desirable in ambient noise tomography applications [e.g., *Shapiro et al.*, 2005]. This, in turn, means that the cross correlations will amplify signal coherence between the two stations at a lag corresponding to the source-station traveltime differences. The side of $\Delta t = 0$ where the correlations align is determined by which station of the pair is closer to the noise source. In all three examples of noise correlation shown in Figures 5–7, the signals at C16A lag those observed

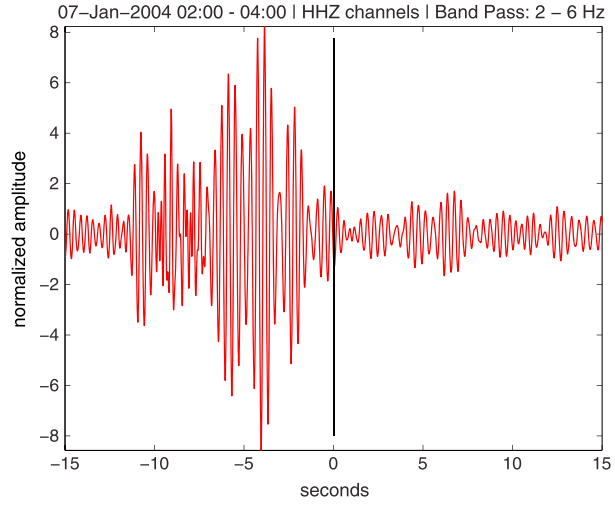

Figure 6. Noise correlation function $\mathcal{X}$ (nondimensional) for a 2 h time window on 7 January 2014 between stations C16B and C16A and band pass filtered to 2–6 Hz. C16A's noise appears to have an approximately 2–10 s lag relative to that for C16B in this example, as is evident from the increase in amplitude of the noise correlation function aligned within a band of Δt from −2 to −10 s.

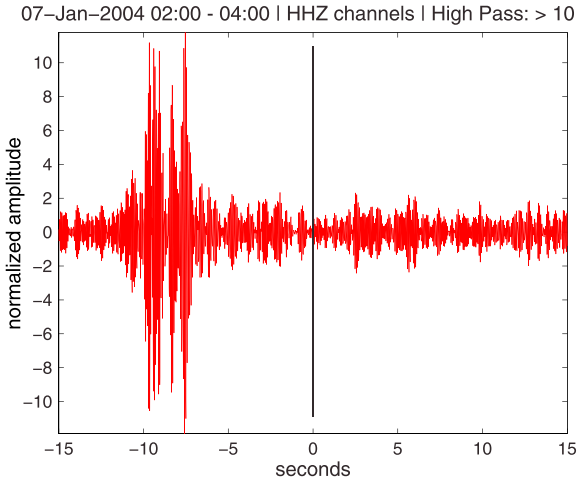

Figure 7. Noise correlation function $\mathcal{X}$ (nondimensional) for a 2 h time window on 7 January 2014 between stations C16B and C16A and high pass filtered to > 10 Hz. C16A's noise appears to have an approximately 8–10 s lag relative to that for C16B in this example, as is evident from the increase in amplitude of the noise correlation function aligned within a band of Δt from −8 to −10 s.

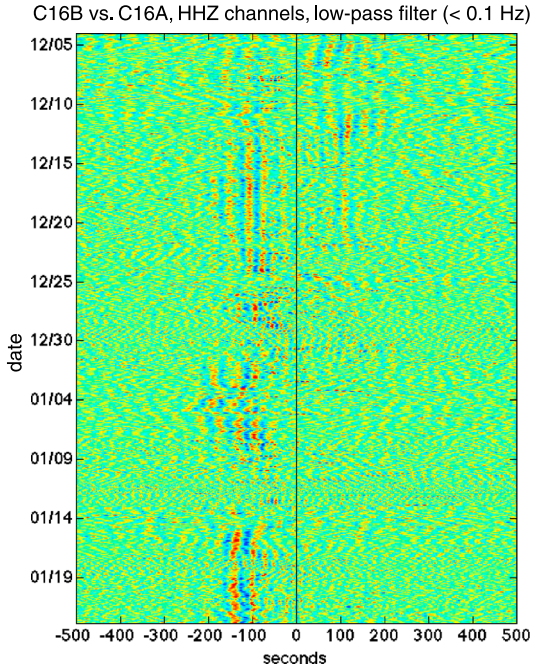

Figure 8. Noise correlation time series $\mathcal{X}_n$ (nondimensional) for $n = 1, \ldots, 600$ covering 50 days of HHZ records from C16B and C16A low pass filtered to below 0.1 Hz. The color scale here and on subsequent figures designates where correlations are positive (red) and negative (blue); otherwise, the magnitude of the color scale is arbitrary and chosen to highlight the presence of strong-amplitude signals (oscillations between red and blue) in the nondimensional (normalized) noise correlation function $\mathcal{X}$.

at C16B, and this is consistent with our expectation that the iceberg collision zone near C16B is the source of the noise.

The filtered noise correlation functions shown in Figures 5–7 display what we believe to be at least three, and possibly four, phases of wave propagation. At low frequency (Figure 5), the function displays an approximately 50 s period signal beginning at a time lag of about −100 s that is distinct in its periodicity from the noise correlation prior to −200 s and after −100 s. For a noise source near station C16B (as we shall show below), and with C16A being about 12 km farther from the source than C16B, the −100 s time lag implies a phase speed of roughly 120 m s^{-1}. The 2–6 Hz band-filtered noise correlation function shown in Figure 6 displays a diffuse signal in a range of time lags between −2 s and −10 s. Assuming a noise source near C16B (again, to be justified below), these time lags imply fast phase propagation covering the extra 12 km source-to-station distance associated with C16A relative to C16B at speeds in an approximate range of 1200–6000 m s^{-1}. Finally, the high-pass-filtered function (Figure 7) displays a signal that is located at a time lag strictly below −8 s. The phase propagation speed implied by this time lag is roughly 1500 m s^{-1}, again assuming that the noise source is near C16B.

To explore how noise correlation functions varied over the 60 day period of seismometer deployment, we computed time series of the 2 h time window noise correlation functions. For C16A and C16B, the noise correlation time series extended through 50 days of operation and gave $N = 600$ elements in the time series. Figures 8–10 display the time series of noise correlation functions for stations C16A and C16B, for data channels HHZ, and low pass filtered (<0.1 Hz), band pass filtered (2–6 Hz), and high pass filtered (> 10 Hz), respectively. In Figure 11, we display subsets of the time series shown in Figures 9 and 8 to emphasize two types of apparent diurnal rhythm in the noise correlation functions.

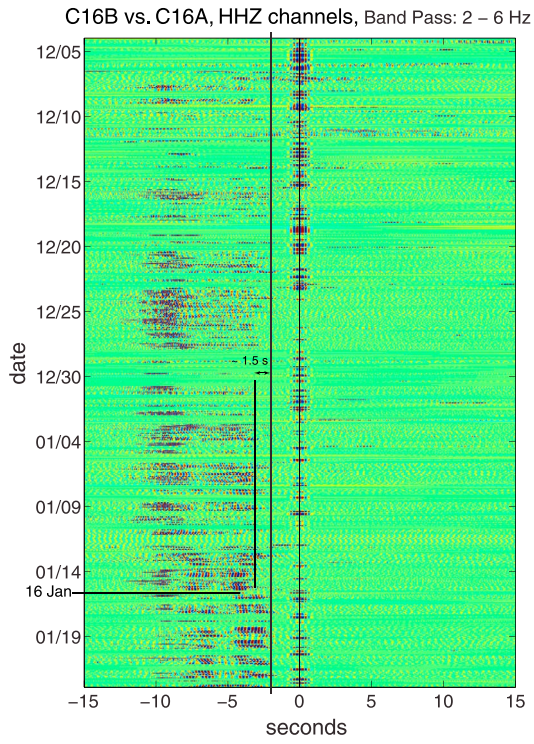

Figure 9. As in Figure 8 but band pass filtered to 2–6 Hz. Vertical lines are drawn at approximately 0 s, −2.0 s, and −3.5 s to assist in visualizing the alignment of noise correlation and secular changes in this alignment (at roughly 16 January 2004) over the course of the 50 day observation period.

The noise correlation time series shown in Figures 8–10 indicate the two important characteristics previously noted in our discussion of the single 2 h time window noise correlation functions: first, the noise correlation functions are not symmetric about $\Delta t = 0$, and this is indicative of a discrete noise source, and second, the noise correlation functions display signals at multiple time lags depending on the frequency filter, and this is indicative of multiple phases of propagation. We note two other characteristics of the noise correlation function time series, one physical and one an artifact of data processing. The physical characteristic is the approximate diurnal periodicity in the noise correlation signals when filtered into the 2–6 Hz band or above 10 Hz. This diurnal periodicity will be discussed below. The unphysical aspect of the time series is characterized by the fact that a strong signal appears near 0 s time lag for some of the data windows. Further investigation (not shown) revealed that these apparent 0 s time correlations were associated with data windows in which the ambient noise amplitude was extremely low, 3 orders of magnitude (in ground velocity) below the magnitude of ambient noise associated with data windows where the 0 s signal was dominated by signals at other, more meaningful time lags. This apparent 0 s signal was further found to be sensitive to time series filter details. The apparent 0 s lag signal is thus simply an artifact of the data analysis that is overemphasized in Figures 8–10. The overemphasis stems from the normalization of the noise correlation functions by their standard deviation within each data window (i.e., division by σ_n in equation (1)). This means that the nearly noise-free data windows with the 0 s lag spurious signal are displayed at the same scale as the results for data windows where the ambient noise magnitude was strong.

Diurnal rhythms of the noise correlation functions are shown in Figure 11. In Figure 11a, noise correlation signals filtered to the 2–6 Hz band tend to group into packages that are separated by quiet periods (with little or no noise correlation) occurring approximately once a day. This is consistent with the fact that the motion of iceberg B15A, whose collisions with C16 are the presumed source of iceberg tremor that dominates the ambient noise on C16 within the 2–6 Hz band, was strongly driven by the predominant diurnal tide of the Ross Sea [*MacAyeal*, 1984]. Another notable secular change in the noise correlation time series is viewed in Figure 9, where there appears to be a shift in the time lag associated with the earliest noise signal arriving at C16A (the shift is highlighted by the two vertical lines in Figure 9). Although this shift can be seen as ambiguous by some eyes, it appears as though the signal arrives about 1.0 s to 1.5 s earlier in the time period after 16 January relative to the time period before. We do not know the reason for this change but speculate that it could be due to a change of the geometry of B15A and B15J relative to C16 during the period of seismometer deployment [*MacAyeal et al.*, 2008a] (see also Figure 1). A shift in the iceberg collision zone leading to a reduction of the source-to-station distance for C16A relative to C16B by 1.5 km, for example, could explain the change in signal time lag.

Figure 11b shows a diurnal periodicity in the noise correlation function in the < 0.1 Hz band. This periodicity is characterized by an approximate 10 s shift in the time lag Δt that characterizes the noise correlation

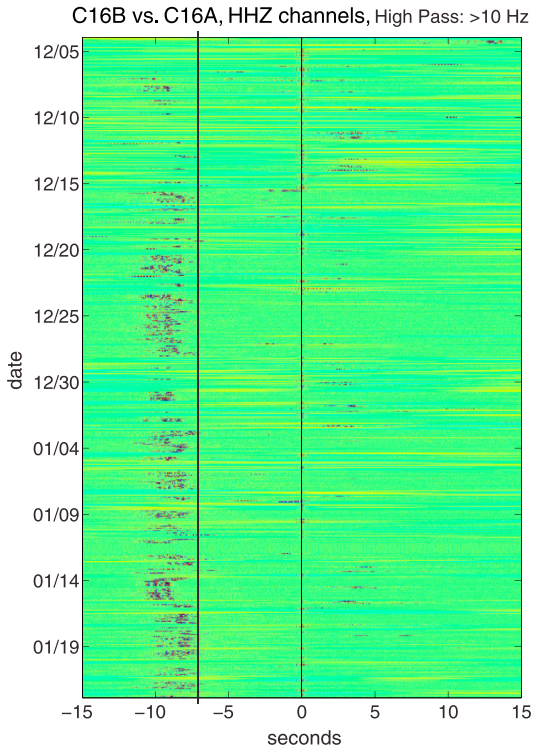

Figure 10. As in Figure 8 but high pass filtered to above 10 Hz. Vertical lines are drawn at approximately 0 s and −7.0 s to assist in visualizing the alignment of noise correlation and secular changes in this alignment over the course of the 50 day observation period.

function's dominant signal. The arrival time of this wave averages around −100 s, which corresponds to a flexural gravity wave [e.g., *Williams and Robinson*, 1979; *Squire et al.*, 1994; *Cathles et al.*, 2009; *Sergienko*, 2010, 2013; *Bromirski et al.*, 2010] propagating an extra 10 km or so (at the shallow water gravity wave speed of $\sqrt{gH} = \sim 94\ \mathrm{m\,s^{-1}}$, where g is the acceleration of gravity and H is water depth, appropriate for $H = 900$ m) to reach C16A after it reaches C16B. The approximate 10 s shift in this arrival time suggests that the location of the source is shifting on a diurnal basis, e.g., driven by the diurnal tide, to add an additional 1 km to the extra travel distance between C16B and C16A. This addition of extra travel distance is fully consistent with the source being long-period ocean waves radiating from B15A which was moving on the order of several kilometers during each tidal cycle [*MacAyeal*, 1984]. What is perhaps most important is the change of the azimuth between station midpoint and source, as this will have the most direct influence on the relative source-station distances.

With four stations and three components of ground motion, a set of $12 \times 12 = 144$ cross-correlation and autocorrelation functions can be computed from our data for any time window. We display a subset of the 144 averaged noise correlation functions, $\bar{\mathcal{X}}(\Delta t)$, in Figure 12. In Figure 12, we present the noise correlation for three spatial components, EE, NN, and ZZ, filtered into the same frequency bands as in the analysis of the noise correlation time series discussed above: low pass below 0.1 Hz, band pass between 2 and 6 Hz, and high pass above 10 Hz. In Figures 12a and 12b, we present the results for C16A and C16B; in Figure 12c, we present results for C16A and C16D.

The average noise correlation functions, $\bar{\mathcal{X}}(\Delta t)$, in Figure 12 reveal several of the same characteristics as determined from inspection of the noise correlation time series in Figures 8–10: that the noise correlation functions are not symmetric about $\Delta t = 0$ and that the time lags of the cross-correlation maxima (i.e., arrival time differences) are a function of frequency. Furthermore, as evident in Figure 12b's depiction of the ZZ channels in the 2–6 Hz band, there appear to be two peaks of amplitude where the correlation function is strong, one centered at ∼−4 s and the other centered at ∼−8 s. Unfortunately, it was not possible to separate these two peaks by experimenting with the time series filters; hence, it remains somewhat speculative that there are two separate peaks. A final point of casual inspection reveals that the ZZ channel correlation shown in Figure 12c, depicting the low-frequency content of the $\chi(\Delta t)$, displays a signal centered at Δt ∼90 s. The fact that this correlation is not shown in the EE and NN channels (however, correlations at smaller lags are still shown) draws attention to the possibility of a mode that travels very slowly from its source and which involves primarily vertical motion.

4. Interpretation

Interpretation of the noise correlation functions shown in the previous section is rendered imprecise because the ice thickness of the iceberg is largely unknown, as are the iceberg's density and thermal structure. This means that it is difficult to interpret specific characteristics seen in the noise correlation functions in terms of well-defined seismic and hydroacoustic wave types. The three interpretations of the system that we believe to be most strongly supported by the data are the following: (1) that the ambient

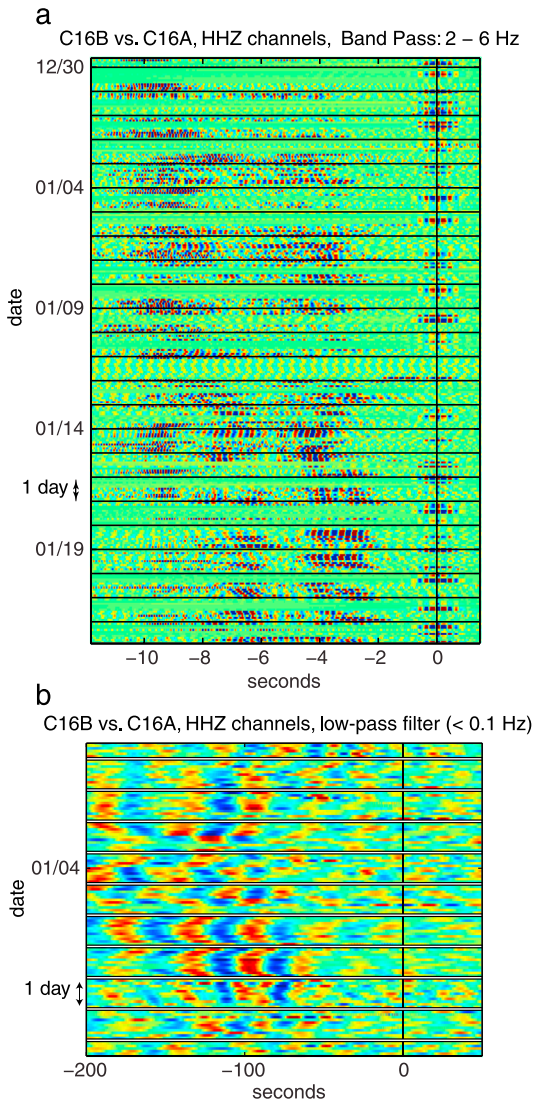

Figure 11. Subset of the noise correlation time series shown in Figures 9 and 8. Horizontal lines are drawn each day of the record to demonstrate the apparent diurnal variation in (a) noise correlation amplitude $|\mathcal{X}|$ and (b) time lag Δt. Diurnal variation in amplitude of the 2–6 Hz band suggests that noise generated by iceberg collisions (iceberg tremor) is modulated by when the predominant diurnal ocean tide dictates that B15A is in contact with C16 as shown in Figure 11a. Diurnal variation in the time lag of the ~30–50 s period oscillation in the noise correlation function is about 10–15 s as shown in Figure 11b.

noise field is dominated by seismic noise generated in the iceberg collision zone that is spatially constrained to within a few kilometers during the period of deployment; (2) that at high frequency (>10 Hz), the noise is propagated primarily as a hydroacoustic mode trapped within the water column between the ice and the seabed; and (3) at periods below 10 s, the noise field is dominated by long-period gravity waves which again appear to originate from a single compact source consistent with the presence of B15A and B15J in the region surrounding C16.

The existence of a dominant noise source located within the iceberg collision zone (Figure 1) is the easiest interpretation to make because, aside from being expected from independent information [*MacAyeal et al.*, 2008a], the noise correlation functions are all asymmetric with respect to Δt and lagged in a manner consistent with the station geometry and station distances from the collision zone. The localization of the noise source means that the noise correlation functions do not converge toward station-to-station impulse response functions as is ideal for ambient noise tomography [e.g., *Zhan et al.*, 2014].

To demonstrate the existence of a dominant noise source, we examined an array of point locations, both within and outside of the region occupied by C16, to determine the location that is most consistent with the observed time lags for high-frequency (> 10 Hz) signals received at all the stations. For this, we assume (a priori) that (a) the high-frequency signal is a hydroacoustic mode (support for this assumption is discussed further below); (b) the phase propagation speed in water at near freezing temperature is 1460 m s^{-1}; (c) the path of propagation involves a reflection off a seabed with a depth of 800 m (given the large horizontal distances between the determined source and the stations, treatment of reflection from the seabed was not critical to the analysis); (d) the noise source is at the surface of the ocean; and (e) the traveltime for the converted hydroacoustic wave in the iceberg itself is negligible because the iceberg is so thin (~50–75 m). To perform this computation, we first computed all the Δt times of the presumed hydroacoustic signals by picking by eye where the signal first appears on the side of the $\mathcal{X}(\Delta t)$ function closest to $\Delta t = 0$. Next, a least squares performance function was evaluated at each of all grid cells on a 1 km by 1 km grid containing the iceberg, based on the difference between a modeled set of signal Δt times and those observed (and picked by eye) in the data. This performance function is presented in Figure 13. The minimum value of the performance function is indeed located near the edge of the iceberg in the collision zone, where B15A was observed to

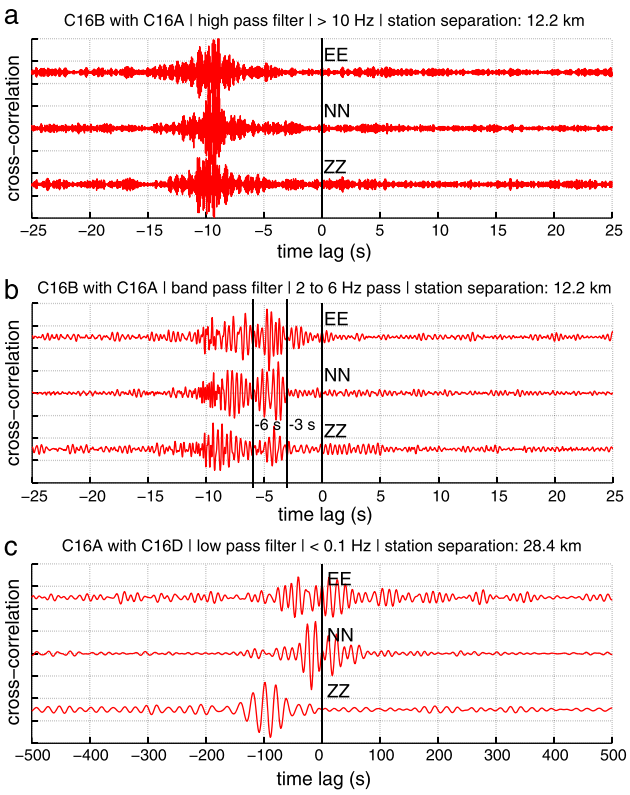

Figure 12. Noise correlation functions averaged for the entire data collection period, $\bar{\mathcal{X}}$. (a) Station C16B with C16A filtered (high pass, 10 Hz) to show hydroacoustic phase. Cross correlations of E, N, and Z seismometer channels are denoted by EE, NN, and ZZ, respectively, and are offset vertically (arbitrary scale) from each other for better display. (b) Station C16B with C16A, as in Figure 12a but band pass filtered (2–6 Hz) to display seismic (possibly *P*- and *S*-like) phases. (c) Stations C16A and C16D, as in Figure 12a but band pass filtered (from 1 s sample rate LH* data) to 0.05 to 0.1 Hz to display a possible flexural gravity wave phase (visible in ZZ noise correlation function only).

frequently collide with C16 [*MacAyeal et al.*, 2008a]. The subjectivity of this picking procedure is up to several seconds. However, repeated trials of the picking procedure did not seem to strongly influence the inferred location.

At frequencies above about 10 Hz, the noise correlation functions are most consistent with hydroacoustic propagation in the water column below the iceberg at the phase speed of approximately 1460 m s^{-1}, which is expected for water temperatures of −1.9°C. Our interpretation of hydroacoustic propagation is supported by record sections created with the noise correlation functions shown in Figure 14a. When the six independent noise correlation functions possible for a four-station array are arranged according to difference in source-station distance (assuming the source locates in the collision zone), the functions display large-amplitude signals aligned along a line roughly consistent with a 1460 m s^{-1} phase speed.

A second feature in the noise correlation functions that is consistent with hydroacoustic propagation in the water column is what we believe to be a low-frequency cutoff visible in some of the station pairs. As shown in Figure 14b, where the functions are filtered to the 2–6 Hz band, many of the stations appear to have lost a strong signal that is aligned with the 1460 m s^{-1} phase speed line (most notably station pairs C16D-C16C, C16C-C16B, and C16C-C16A, which involve stations C16D and C16C, where water depth is shallow). To explain the disappearance of the hydroacoustic signal above ~6 Hz, we consider the nature of the water layer below the iceberg. This layer constitutes a waveguide of minimum velocity, bounded at the top by the solid ice and at the bottom by the solid earth, both of which feature *P* wave velocities greater than the speed of sound in water. In this respect, the situation is conceptually equivalent to that prevailing in the SOFAR channel [*Ewing and Worzel*, 1948], even though the details of the distribution of velocities with depth may differ.

In order for a layer of minimum velocity to act as an efficient waveguide, the frequency of the wave must be high enough to fit a single wavelength inside the vertical thickness of the channel. This means that there is a long-wavelength cutoff equal to the water column thickness between the iceberg and the seabed. This thickness is variable, ranging from about 900 m below C16B to near 0 m at C16C and C16D, where the iceberg is aground. Taking 250 m as a representative water column thickness below the iceberg along the path from C16D to C16C, and using a sound velocity of ~1460 m s^{-1}, the low-frequency cutoff is at about $f_c \approx 1460/250 = 5.8$ Hz. This lends support to the interpretation that the high-frequency part of the noise correlation functions represents a hydroacoustic phase within the water column.

The most difficult part of the noise correlation functions to interpret is the apparent propagation of wave modes that have velocities approaching what is expected for seismic waves in ice. The record section shown

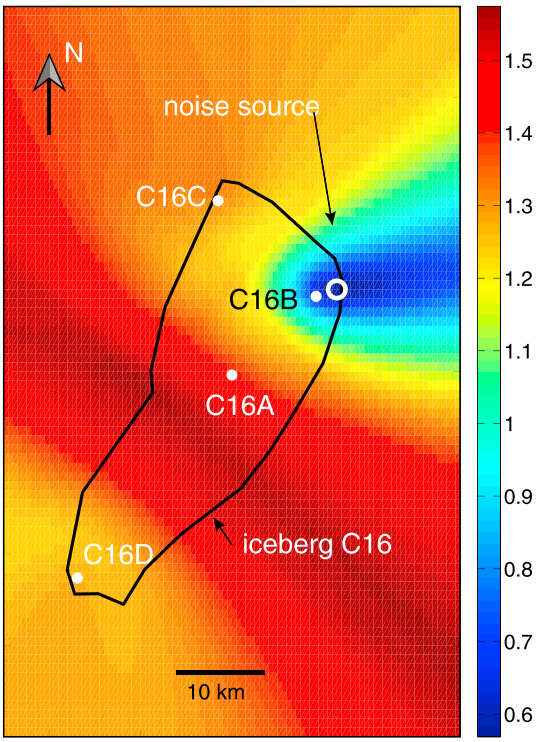

Figure 13. Log of the least squares model/data misfit function. The minimum value of the misfit function (dark blue) occurs near the edge of the iceberg at a location where C16 and B15A collide. Seismic stations are indicated by white dots. The black outline is a digitization of the iceberg border from the MODIS image shown in Figure 1.

in Figure 14b shows significant amplitude propagating with a phase speed that is between about ~3000 m s^{-1} and the hydroacoustic mode at ~1460 m s^{-1}. The noise correlation functions do not show a distinct gap of low amplitude between the fast mode and the hydroacoustic mode; hence, it is impossible for us to determine whether there are separate seismic phases that are distinct from the hydroacoustic phase, e.g., as observed on another iceberg by *Hunkins* [1960], or whether there is simply a combined seismic/hydroacoustic mode that becomes more seismic at low frequency (where the water column waveguide has a cutoff) and more hydroacoustic at high frequency. Examining the C16B/C16A $\chi(\Delta t)$ values filtered into the 2 Hz to 6 Hz band (Figure 12b), we interpret there to be two signals at $\Delta t \sim -6$ s and ~ -4 s. The presence of two signals is consistent with what was observed by *Hunkins* [1960], who conducted both active and passive seismic experiments on a tabular iceberg in the Arctic Ocean. He found that there were both longitudinal and shear modes of wave propagation within the iceberg and that these had phase velocities in the ranges of ~2400 to ~3100 m s^{-1} and ~1550 to ~1850 m s^{-1}, respectively. The phase velocity variation on the iceberg was found to be associated with ice temperature and varied through the seasonal cycle. *Zhan et al.* [2014] also noted two distinct ambient noise correlation signals on the Amery Ice Shelf. They interpreted the slowest signal in the 1 Hz to 5 Hz band as a Rayleigh wave in the ice shelf that was influenced by a low-velocity firn layer.

5. Discussion and Conclusions

The application of noise correlation analysis to the data collected by four seismic stations on iceberg C16 has identified at least three modes of wave propagation across the iceberg. This demonstrates a considerable benefit of noise correlation analysis, because, on icebergs, there appear to be relatively few icequake-type signals amenable to more traditional arrival time-type analysis. The main benefit of noise correlation we found in our study was that it allowed us to identify multiple phases of wave propagation (i.e., seismic, hydroacoustic, and flexural gravity wave) from a localized source that demonstrated both diurnal and multiday temporal evolution. Specifically, we see that the high-frequency signals are consistent with iceberg tremor, are propagated as hydroacoustic waves in the water between the iceberg and seabed, and are modulated by the diurnal tide, which controls collisions between iceberg C16 and B16A. As an aside, we note that there are other cases where unusual field deployments of seismic arrays have led to similar results. As demonstrated by *Larose et al.* [2005], the deployment of a four-seismograph array on the lunar surface at the Apollo 17 landing site was also amenable to noise correlation analysis, which led to analogous results: the noise had a dominant localized source (a nearby crater) and was modulated by the lunar diurnal cycle (due to thermal sources of seismicity).

Unlike the results from another seismic array deployment on floating ice [*Zhan et al.*, 2014], where noise correlation functions converged (at least in the low-frequency regime) toward station-to-station impulse response functions, ambient noise tomography was not possible in our study using the same methodology. This does not rule out the possibility that such an analysis could be done with other methods or in other

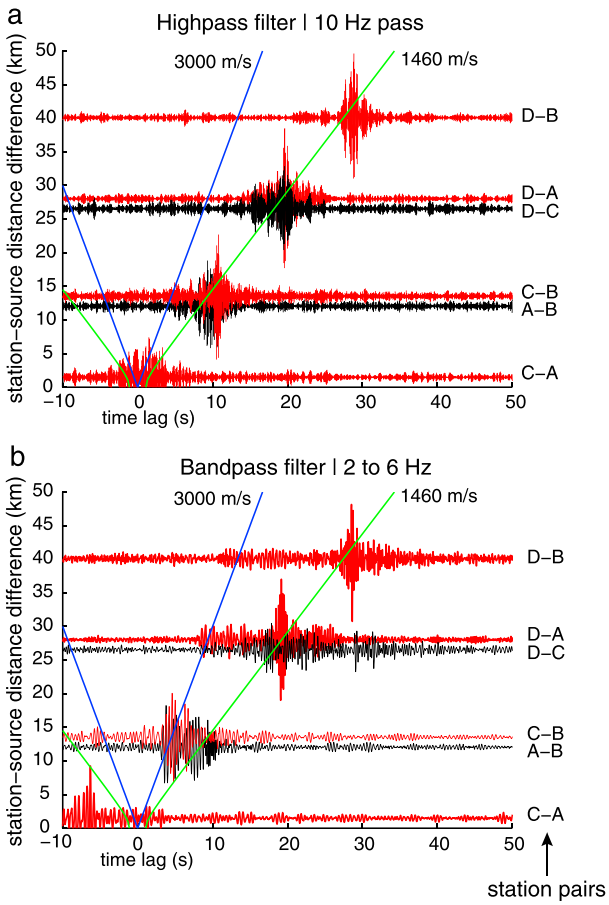

Figure 14. Record sections of noise correlation functions (HHZ channels) using station-source distance difference. (a) High-pass-filtered data showing hydroacoustic modes. (b) Band-pass-filtered data to show what appear to be *P*- and *S*-like propagation modes in the iceberg. Phase propagation lines with arbitrarily chosen velocities of 3000 and 1460 m s^{-1} are displayed to assist in visualizing what appear to be distinct seismic and hydroacoustic modes of propagation.

field settings where floating ice is surrounded by a noise-producing environment that is dispersed spatially. We suggest that further deployments are warranted to investigate the potential for ambient noise tomography in glaciologically significant field settings, e.g., near grounding lines where important changes in seawater migration caused by tidal forcing may be determined from the otherwise diffuse field of seismic rumblings that accompany grounding line ice dynamics [e.g., *Pratt et al.*, 2014; *Lipovsky et al.*, 2014].

The diurnal pulsation of ambient noise energy shown in Figure 11 and the apparent shift in the onset of signal in the noise correlation function time series around 16 January seen in Figure 9 both suggest that the properties of the noise field functions are responding to changes in the environment and especially to factors controlling the noise source. This may turn out to be useful in understanding what is now recognized as a dominant source of ocean hydroacoustic noise. *Matsumoto et al.* [2014] have shown that acoustic emanations associated with the drift and decay of Antarctic icebergs are the dominant source for hydroacoustic noise in all of the Southern Hemisphere's oceans. They found that this noise is modulated by the seasonal cycle and attributed this modulation to the effect of surface melting on iceberg decay and breakup. To better understand this noise, and to characterize it at its source, it may be necessary to deploy more sensors on drifting icebergs and to use noise correlation analysis to interpret their data. At the very least, the results of our single deployment of a seismometer array on a partially grounded iceberg show that generation and transmission of hydroacoustic noise from an iceberg source are entirely consistent with icebergs being the source of hydroacoustic noise more generally in the Southern Ocean.

Based on our experience with ambient noise on C16, we speculate that noise correlation analysis has the potential to be useful in other glaciological settings where distinct icequake-type signals may be difficult to find and where there may be long-term changes in seismic and hydroacoustic properties influenced by ice dynamics and climate change. We have shown that flexural gravity waves are evident in the noise signals on the iceberg. By following the example set by *Marsan et al.* [2012], who use flexural gravity wave noise to measure sea ice thickness, ambient noise analysis may prove to be useful as a means to monitor and identify long-term changes of an iceberg or ice shelf that may accompany basal melting, surface firn densification, surface melting, and crevasse damage. Another possible application of noise correlation monitoring would be the study of subglacial lakes, where subtle changes in the low-frequency cutoff for hydroacoustic propagation in a subglacial lake waveguide could help to determine the lake's depth over time. We thus recommend additional study into noise correlation analysis of seismic signals in the cryosphere as a means to investigate two essential elements of how ice sheets may be forced by climate change.

Acknowledgments
We thank three referees (two anonymous and Fabian Walter) and the Scientific Editor for their substantial help with improvement of both the scientific analysis and several versions of the manuscript. Field work component of this research was supported by NSF grant OPP-0229546; analysis work was supported by NSF grants ANT-0944233 and ANT-0944193. For assistance in the field, we thank Raytheon Polar Services Co., PHI and Ken Borek aircraft services, Tim Parker of PASSCAL and Marianne Okal. Data used in this study are publicly available for download from the DMC of IRIS (http://www.iris.edu/mda/XV?timewindow=2003-2006). Ronald Ross designed and deployed the autonomous camera system that overlooked the collision zone near seismic station C16B used to create the time lapse video available in the supporting information.

References

Bromirski, P. D., O. V. Sergienko, and D. R. MacAyeal (2010), Transoceanic infragravity waves impacting Antarctic ice shelves, *Geophys. Res. Lett.*, *37*, L02502, doi:10.1029/2009GL041488.

Cathles, L. M., E. A. Okal, and D. R. MacAyeal (2009), Seismic observations of sea swell on the floating Ross Ice Shelf, Antarctica, *J. Geophys. Res.*, *114*, F02015, doi:10.1029/2007JF000934.

Ewing, M., and J. L. Worzel (1948), Long-range sound transmission, *Geol. Soc. Am. Mem.*, *27*, 1–32, doi:10.1130/MEM27-3-p1.

Hadziioannou, C., E. Larose, A. Baig, P. Roux, and M. Campillo (2011), Improving temporal resolution in ambient noise monitoring of seismic wave speed, *J. Geophys. Res.*, *116*, B07304, doi:10.1029/2011JB008200.

Hunkins, K. (1960), Seismic studies of sea ice, *J. Geophys. Res.*, *65*(10), 3459–3472, doi:10.1029/JZ065i010p03459.

Larose, E., A. Khan, Y. Nakamura, and M. Campillo (2005), Lunar subsurface investigated from correlation of seismic noise, *Geophys. Res. Lett.*, *32*, L16201, doi:10.1029/3005GL023518.

Lipovsky, B., D. Olivo, and E. Dunham (2014), Constraints on subglacial conditions from seismicity, Abstract C41C-02 presented at 2014 Fall Meeting, AGU, San Francisco, Calif., 15-20 Dec.

MacAyeal, D. R. (1984), Numerical simulations of the Ross Sea tides, *J. Geophys. Res.*, *89*(C1), 607–615, doi:10.1029/JC089iC01p00607.

MacAyeal, D. R., M. H. Okal, J. E. Thom, K. M. Brunt, Y. J. Kim, and A. K. Bliss (2008a), Tabular iceberg collisions within the coastal regime, *J. Glaciol.*, *54*(185), 371–386, doi:10.3189/002214308784886180.

MacAyeal, D. R., E. A. Okal, R. C. Aster, and J. N. Bassis (2008b), Seismic and hydroacoustic tremor generated by colliding icebergs, *J. Geophys. Res.*, *113*, F03011, doi:10.1029/2008JF001005.

Marsan, D., J. Weiss, E. Larose, and J.-P. Métaxian (2012), Sea-ice thickness measurement based on the dispersion of ice swell, *J. Acoust. Soc. Am.*, *131*(1), 80–91, doi:10.1121/1.3662051.

Matsumoto, H., D. R. Bohnenstiehl, J. Tournadre, R. P. Dziak, J. H. Haxel, T-K. A. Lau, M. Fowler, and S. A. Salo (2014), Antarctic icebergs: A significant natural ocean sound source in the Southern Hemisphere, *Geochem. Geophys. Geosyst.*, *15*, 3448–3458, doi:10.1002/2014GC005454.

Pratt, M. J., J. P. Winberry, D. A. Wiens, S. Anandakrishnan, and R. B. Alley (2014), Seismic and geodetic evidence for grounding-line control of Whillans Ice Stream stick-slip events, *J. Geophys. Res. Earth Surf.*, *119*, 333–348, doi:10.1002/2013JF002842.

Sergienko, O. V. (2010), Elastic response of floating glacier ice to impact of long-period ocean waves, *J. Geophys. Res.*, *115*, F04028, doi:10.1029/2010JF001721.

Sergienko, O. V. (2013), Normal modes of a coupled ice-shelf/sub-ice-shelf cavity system, *J. Glaciol.*, *59*(213), 76–80, doi:10.3189/2013JoG12J096.

Shapiro, N. M., M. Campillo, L. Stehly, and M. H. Ritzwoller (2005), High-resolution surface-wave tomography from ambient seismic noise, *Science*, *307*(5715), 1615–1618, doi:10.1126/science.1108339.

Squire, V. A., W. H. Robinson, M. Meylan, and T. G. Haskell (1994), Observations of flexural waves on the Erebus Ice Tongue, McMurdo Sound, Antarctica, and nearby sea ice, *J. Glaciol.*, *40*(135), 377–385, doi:10.1016/S0012-821X(02)00867-1.

Talandier, J., O. Hyvernaud, E. A. Okal, and P.-F. Piserchia (2002), Long-range detection of hydroacoustic signals from large icebergs in the Ross Sea, Antarctica, *Earth Planet. Sci. Lett.*, *203*(1), 519–534, doi:10.1016/S0012-821X(02)00867-1.

Talandier, J., O. Hyvernaud, D. Reymond, and E. A. Okal (2006), Hydroacoustic signals generated by parked and drifting icebergs in the Southern Indian and Pacific Oceans, *Geophys. J. Int.*, *165*(3), 817–834, doi:10.1111/j.1365-246X.2006.02911.x.

Wang, Y.-T. (2014), Analysis of seismic signals within a tabular iceberg, MS thesis, 60 pp., Univ. of Chicago, Chicago, Ill., 14 June.

Williams, R. T., and E. S. Robinson (1979), Ocean tide and waves beneath the Ross Ice Shelf, *Antarct. Sci.*, *203*(4379), 443–445, doi:10.1016/S0012-821X(02)00867-1.

Zhan, Z., V. C. Tsai, J. M. Jackson, and D. Helmberger (2014), Ambient noise correlation on the Amery Ice Shelf, East Antarctica, *Geophys. J. Int.*, *196*(3), 1796–1802, doi:10.1093/gji/ggt488.